ACS central science

http://pubs.acs.org/journal/acscii

Research Article

Allosteric Regulation of IGF2BP1 as a Novel Strategy for the Activation of Tumor Immune Microenvironment

Yang Liu, Qiang Guo, Heng Yang, Xiao-Wen Zhang, Na Feng, Jing-Kang Wang, Ting-Ting Liu, Ke-Wu Zeng,* and Peng-Fei Tu*

Cite This: *ACS Cent. Sci.* 2022, 8, 1102−1115

Read Online

ACCESS | Metrics & More | Article Recommendations | Supporting Information

ABSTRACT: Tumor immune microenvironment (TIME) regulators are promising cancer immunotherapeutic targets. IGF2BP1, as a crucial N^6-methyladenosine (m^6A) reader protein, recognizes m^6A target transcripts, ultimately leading to cancer development. However, currently, the biological function of IGF2BP1 in regulating the TIME is not well-understood. In this study, we report that IGF2BP1 knockdown induces cancer cell apoptosis, thereby significantly not only activating immune cell infiltration including $CD4^+$, $CD8^+$ T cells, $CD56^+$ NK cells, and $F4/80^+$ macrophage but also decreasing PD-L1 expression in hepatocellular carcinoma (HCC). Then, chemical genetics identifies a small-molecule cucurbitacin B (CuB), which directly targets IGF2BP1 at a unique site (Cys253) in the KH1−2 domains. This leads to a pharmacological allosteric effect to block IGF2BP1 recognition of m^6A mRNA targets such as *c-MYC*, which is highly associated with cell apoptosis and immune response. In vivo, CuB exhibits an obvious anti-HCC effect through inducing apoptosis and subsequently recruits immune cells to tumor microenvironment as well as blocking PD-L1 expression. Collectively, IGF2BP1 may serve as a novel pharmacological allosteric target for anticancer therapeutics via mediating TIME.

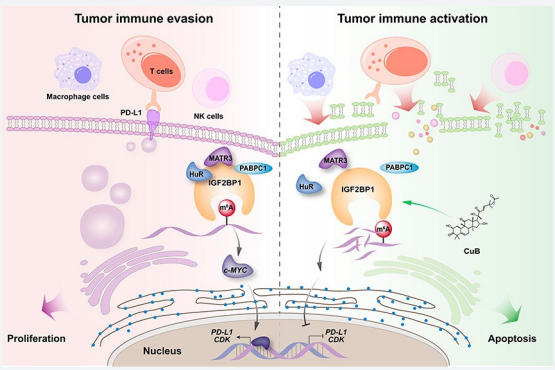

INTRODUCTION

The components of the immune system play a crucial role in combating tumors.[1,2] Despite the firm efforts of these components in the elimination of tumors, tumor cells cleverly escape the surveillance process of the immune system by adopting several immune evasion mechanisms, such as immunosuppression.[3−5] Immune checkpoint inhibitor (ICI) therapy is emerging as a promising therapeutic option for cancer treatment.[6−8] Meanwhile, modulating the immune system with ICIs still faces obstacles with severe immunogenic side effects and a lack of response against many cancer types.[9,10] Therefore, developing small-molecule drugs that trigger antitumor immunity will provide new insight into cancer therapeutics.

As the most abundant messenger RNA (mRNA) modification, N^6-methyladenosine (m^6A) plays diverse roles in various biological processes in eukaryotes.[11,12] Recently, m^6A reader proteins from a distinct family—insulin-like growth factor-2 mRNA-binding proteins (IGF2BPs)—have been reported to directly recognize m^6A modification, thereby promoting the stability and storage of m^6A-modified mRNA by recruiting the cofactors, including ELAV-like RNA binding protein 1 (ELAVL1, also called HuR) and matrin 3 (MATR3).[13] IGF2BPs belong to a highly conserved family of RNA-binding proteins and comprise three major members including IGF2BP1, IGF2BP2, and IGF2BP3. Functionally, IGF2BP1−3 fortify the stability and increase the translation efficiency of m^6A-modified mRNAs, further leading to tumor cell proliferation, invasion, and metastasis.[14−17] However, whether IGF2BPs contribute to tumor immune microenvironment (TIME) regulation is still poorly understood.

IGF2BP1 has been identified to play important roles in regulating mRNA targets, such as *PTEN*, *ACTB*, *MAPK4*, *c-MYC*, and *CD44*, in an m^6A-dependent manner.[18−20] Aberrant IGF2BP1 overexpression in many cancers, particularly in hepatocellular carcinoma (HCC), gallbladder cancer (GC), and breast cancer (BC), is associated with a poor prognosis and shorter survival.[21,22] Therefore, IGF2BP1 is considered to be a promising therapeutic target for cancer treatment. Structurally, IGF2BP1 consists of six canonical RNA-binding domains, including four K homology (KH) domains and two RNA recognition motifs (RRMs).[23] Although the RRM domains of IGF2BP1 can potentially contribute to the

Received: January 28, 2022
Published: May 17, 2022

https://doi.org/10.1021/acscentsci.2c00107
ACS Cent. Sci. 2022, 8, 1102−1115

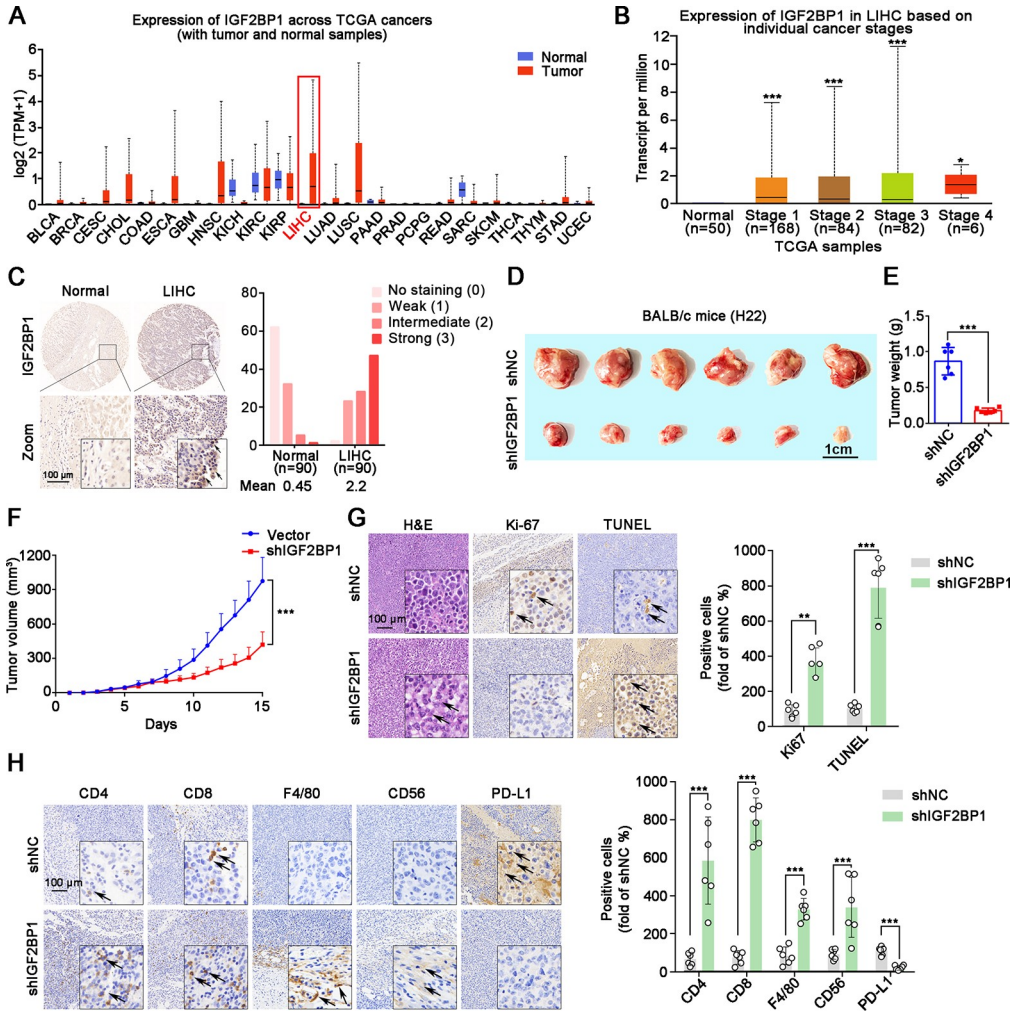

Figure 1. IGF2BP1 knockdown inhibits HCC progression via activating immune cell recruitment and decreasing PD-L1 expression in TIME. (A) IGF2BP1 expression profile across a variety of malignancies compared with normal tissues from the GEPIA database. (B) IGF2BP1 expression levels in LIHC were positively associated with advanced tumor stage determined by TCGA database using UALCAN database. (C) IGF2BP1 expression levels were increased in tumor tissues (n = 90) compared with their matched adjacent nontumoral tissues (n = 90), as shown in representative immunohistochemical images and mean staining scores. Black arrows indicate IGF2BP1 positive staining cells. (D) Images of tumor tissues in IGF2BP1-silenced H22 tumor-bearing mice compared to the shNC group (n = 6). (E) The weight of subcutaneous xenograft tumors (n = 6). (F) The dynamic change of tumor volume in subcutaneous models was shown at two weeks after injection. (G) Representative histological analysis of tumor specimen stained by H&E, Ki-67, and TUNEL (scale bars = 100 μm). Quantification of Ki-67 and TUNEL is shown (n = 6). (H) Representative images of IHC staining for CD4, CD8, F4/80, CD56, and PD-L1 in tumor tissues (scale bars = 100 μm). Quantification of IHC staining is shown (n = 6). Black arrows indicate positive staining cells. Data are shown as mean ± SD. *P < 0.05, **P < 0.01 and ***P < 0.001 vs shNC group.

stabilization of IGF2BP1-RNA complexes in a target-dependent manner, previous studies indicate that RNA binding is majorly facilitated by the KH domains.[24−26] However, it remains unknown whether there are druggable domains in IGF2BP1.

In this study, we utilized a chemical genetics strategy to discover a small-molecule cucurbitacine B (CuB) as a probe specially targeting IGF2BP1. We found that CuB covalently modified IGF2BP1 at a unique Cys253 site, further blocking IGF2BP1−m^{6}A interaction via an allosteric effect on its KH1−2 domains. Then, CuB promoted IGF2BP1-dependent target mRNA instability to induce tumor cell apoptosis, thereby recruiting immune cells to the tumor microenvironment. Collectively, our study reveals that IGF2BP1 serves as a valuable allosteric target for cancer therapeutics by reshaping TIME.

RESULTS

IGF2BP1 Knockdown Inhibits HCC Progression Via Activation of Immune Cell Recruitment and Decrease in PD-L1 Expression in TIME. To explore the potential function of IGF2BP1 in different cancers, we explored clinical samples from the The Cancer Genome Atlas (TCGA) and the Genotype-Tissue Expression (GTEx) databases. Transcriptomics studies in the TCGA database showed that IGF2BP1 mRNA expression was highly increased in a variety of malignancies, especially in liver hepatocellular carcinoma (LIHC) tissues, compared with normal tissues (Figure 1A). Additionally, IGF2BP1 expression was positively associated with an advanced tumor stage, especially in patients with stage 4 (Figures 1B and S1A). Patient tissue biopsy specimens further confirmed that IGF2BP1 expression was increased in LIHC tissues compared with adjacent normal tissues (Figures

https://doi.org/10.1021/acscentsci.2c00107
ACS Cent. Sci. 2022, 8, 1102−1115

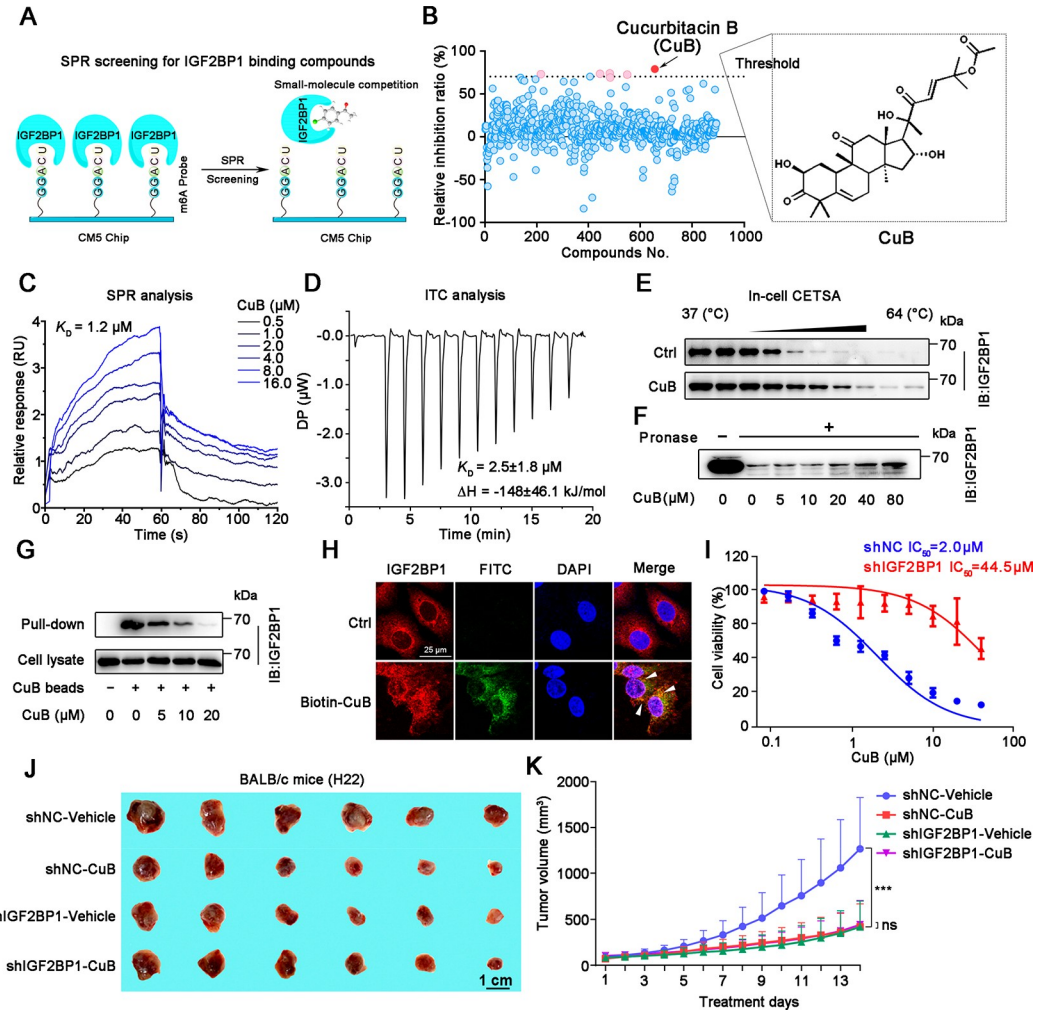

Figure 2. Antihepatocellular carcinoma efficacy of CuB is IGF2BP1-dependent. (A) Schematic diagram of SPR screening for small-molecule disruptors of IGF2BP1-m^{6}A RNA recognition. (B) Inhibition rate of 889 compounds obtained by SPR screening at 10 μM. Black line indicates the criteria (70%). Red points indicate the "hit" candidates of the dose concentrations. Blue points indicate unselected compounds. (C) IGF2BP1 exhibited a potent binding ability with CuB determined by an SPR assay. The kinetic parameter of K_D is derived by fitting to a 1:1 Langmuir binding model. (D) ITC thermograms for the interaction between IGF2BP1-KH1−2 with CuB. (E) CuB promoted the resistance of IGF2BP1 to different temperature gradients by CETSA in Huh7 cells. (F) CuB promoted the resistance of IGF2BP1 to proteases by DARTS in Huh7 cells. (G) Biotin-CuB conjugated beads were incubated with Huh7 cells lysates in the presence or absence of excess CuB. (H) Co-localization of Biotin-CuB (green) and IGF2BP1 (red) by immunofluorescence analysis (bar = 25 μm). White arrows indicate overlapped signals. (I) IGF2BP1 knockdown attenuated the antiproliferative effect of CuB in Huh7 cells. (J) IGF2BP1 knockdown blocked the antiproliferative effect of CuB in BALB/c mice bearing H22 xenografts (n = 6). (K) The dynamic change of tumor volume in subcutaneous models was shown at two weeks after injection. Data are shown as mean ± SD. ***P < 0.001 vs shNC-vehicle group. ns, not significant.

1C and S1B), suggesting that IGF2BP1 may be positively associated with LIHC progression. We therefore hypothesized that IGF2BP1 could serve as a therapeutic target for HCC treatment.

To evaluate the potential role of IGF2BP1 in LIHC progression, we initially established an H22 tumor-bearing model in mice and found that IGF2BP1 knockdown significantly suppressed xenograft tumor growth in BALB/c mice with no obvious change in body and organ weight (Figures 1D−F and S1C,D). As shown in Figure 1G, IGF2BP1 knockdown effectively compromised the structure of HCC cells and reduced K_i-67 positive cell counts, indicating that IGF2BP1 contributed to major effects in tumor cell survival. Terminal deoxynucleotidyl transferase dUTP nick-end labeling (TUNEL) assays revealed that IGF2BP1 knockdown also induced tumor cell apoptosis. Considering that cancer cells undergoing apoptosis usually induce an immune response, we next evaluated the relationship between IGF2BP1 expression and the tumor-infiltrating immune cell response in HCC. Immunohistochemistry (IHC) revealed that IGF2BP1 knockdown resulted in higher percentages of infiltrating CD4$^+$ and CD8$^+$ T cells as well as CD56$^+$ NK cells and F4/80$^+$ macrophage infiltration in tumors (Figure 1H). Since the PD-L1 immune checkpoint also played a crucial role in TIME, we then detected PD-L1 expression. As expected, IGF2BP1 knockdown significantly suppressed PD-L1 expression (Figure 1H). Collectively, these data suggested that IGF2BP1 dysfunction caused cancer apoptosis, thereby leading to antitumor immunity by recruiting tumor-infiltrating immune cells and blocking immunosuppressive factor PD-L1 expression.

Discovery of CuB as an IGF2BP1-Targeting Small Molecule. Our exploration of public databases showed that IGF2BP1 was commonly upregulated in numerous cancer

https://doi.org/10.1021/acscentsci.2c00107
ACS Cent. Sci. 2022, 8, 1102−1115

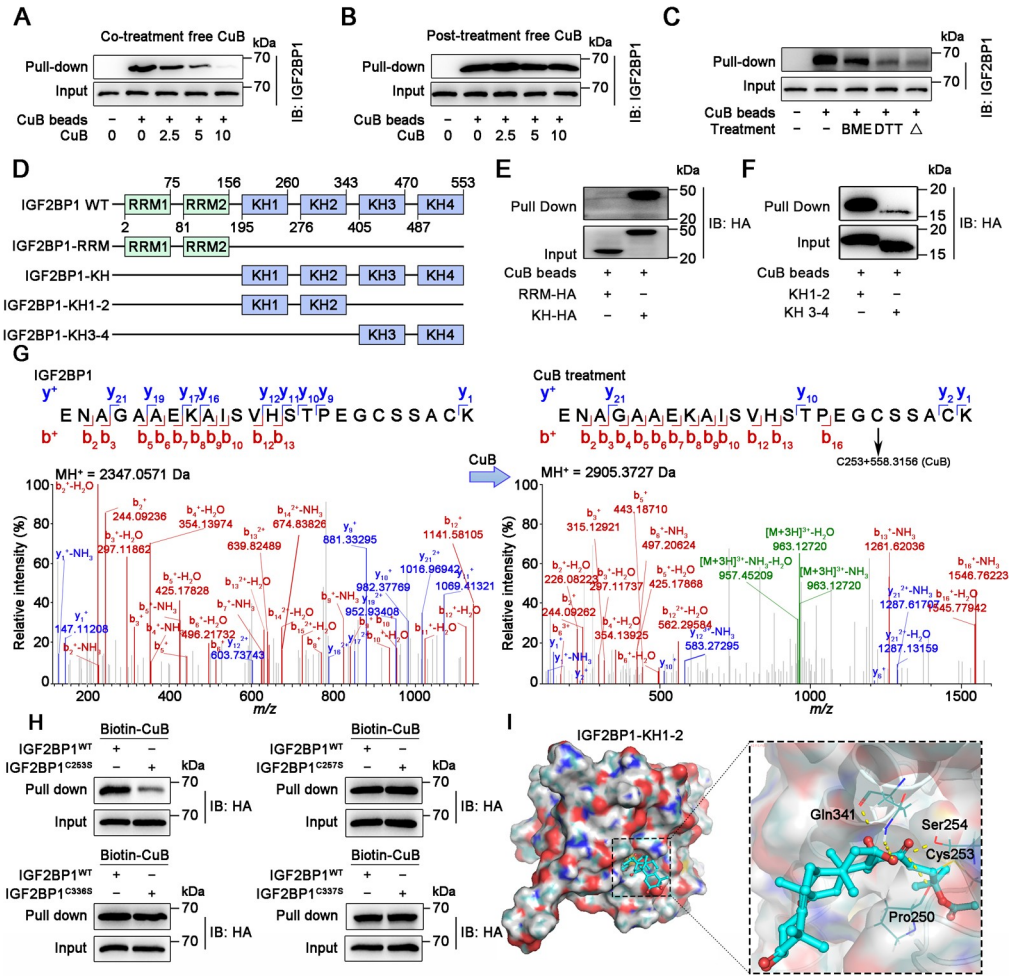

Figure 3. Cys253 is a covalent binding site of IGF2BP1. (A) The recombinant IGF2BP1 protein was incubated with Biotin-CuB beads in the absence or presence of CuB for competitive binding. (B) The recombinant IGF2BP1 protein was preincubated with Biotin-CuB beads for 12 h and then further incubated with or without CuB for competitive binding. (C) Covalent binding of CuB to IGF2BP1. The recombinant IGF2BP1 protein was preincubated with DTT (1 mM) or BME (1 mM) for 2 h (Δ, thermal denaturation) and then further incubated with Biotin-CuB beads at 4 °C for 12 h. (D) Diagrams of IGF2BP1 domains and deletion mutants. (E) CuB interacted with KH domain of IGF2BP1. Recombinant IGF2BP1 mutants were incubated with Biotin-CuB beads at 4 °C for 12 h, and the proteins bound to Biotin-CuB beads were detected by a western blot. (F) CuB interacted with the KH1−2 domain of IGF2BP1. Recombinant IGF2BP1 mutants were incubated with Biotin-CuB beads at 4 °C for 12 h, and the proteins bound to Biotin-CuB beads were detected by a western blot. (G) Typsin-digest LC-MS/MS analysis indicated modification of IGF2BP1 by CuB at residue Cys253. Recombinant IGF2BP1-KH1−2 protein was incubated in the absence (left) or presence (right) of CuB at 4 °C for 12 h. (H) Cys253 mutation blocked the interaction of CuB with IGF2BP1. Recombinant IGF2BP1-KH1−2 protein and its mutants were incubated with Biotin-CuB beads at 4 °C for 12 h. (I) Molecular docking of CuB toward IGF2BP1-KH1−2 (PDB: 6QEY).

types, which can act as an oncogene by promoting the stability, localization, and translation of cancer-related mRNA targets in an m^{6}A-dependent manner. In light of these findings, we therefore sought to identify small molecules that could selectively disrupt the interaction between IGF2BP1 and m^{6}A targets. To this end, we established a high-throughput screening system (Figure 2A). First, we synthesized a methylated single-stranded RNA bait (ss-m^{6}A), with a GG(m^{6}A)CU consensus sequence and an unmethylated control RNA (ss-A) for surface plasmon resonance (SPR) analysis.[27,28] Results showed that the ss-m^{6}A probe specifically bound to IGF2BP1 with a dissociation constant (K_D) of 18.3 nM, almost 13-fold lower than the ss-A probe (Figure S2A,B). Then, high-throughput screening identified six candidates with its inhibitory effect over 70% (Figures 2B and S2C) from a previously established Medicinal Natural Products Library (a total of 889 compounds). A subsequent round of antiproliferative assay on Huh7 cells identified cucurbitacin B (CuB), with a half-maximal inhibitory concentration (IC_{50}) of 4.1, 1.7, and 1.0 μM for 24, 48, and 72 h, respectively (Figure S2D,E). The SPR quantification analysis revealed the strong binding ability of CuB with IGF2BP1 with a dissociation constant (K_D) of 1.2 μM (Figure 2C). We also used isothermal titration calorimetry (ITC) to confirm that CuB directly interacted with IGF2BP1 (K_D = 2.5 μM in a 1:1 ratio; Figure 2D).

Small molecules may increase the protein stability via forming a ligand−protein complex.[29] To determine the effect of CuB on IGF2BP1 stability, we performed cellular thermal shift assays (CETSA) and found that CuB increased IGF2BP1 thermotolerance in a temperature gradient (37−64 °C) (Figure 2E). We next conducted a drug-affinity responsive target stability (DARTS) assay, which revealed that incubation with CuB led to a concentration-dependent increase in IGF2BP1 proteolysis (Figure 2F). To investigate the drug-target engagement of IGF2BP1 in Huh7 cells, we synthesized a biotin-labeled probe (Biotin-CuB) for affinity purification and

https://doi.org/10.1021/acscentsci.2c00107
ACS Cent. Sci. 2022, 8, 1102−1115

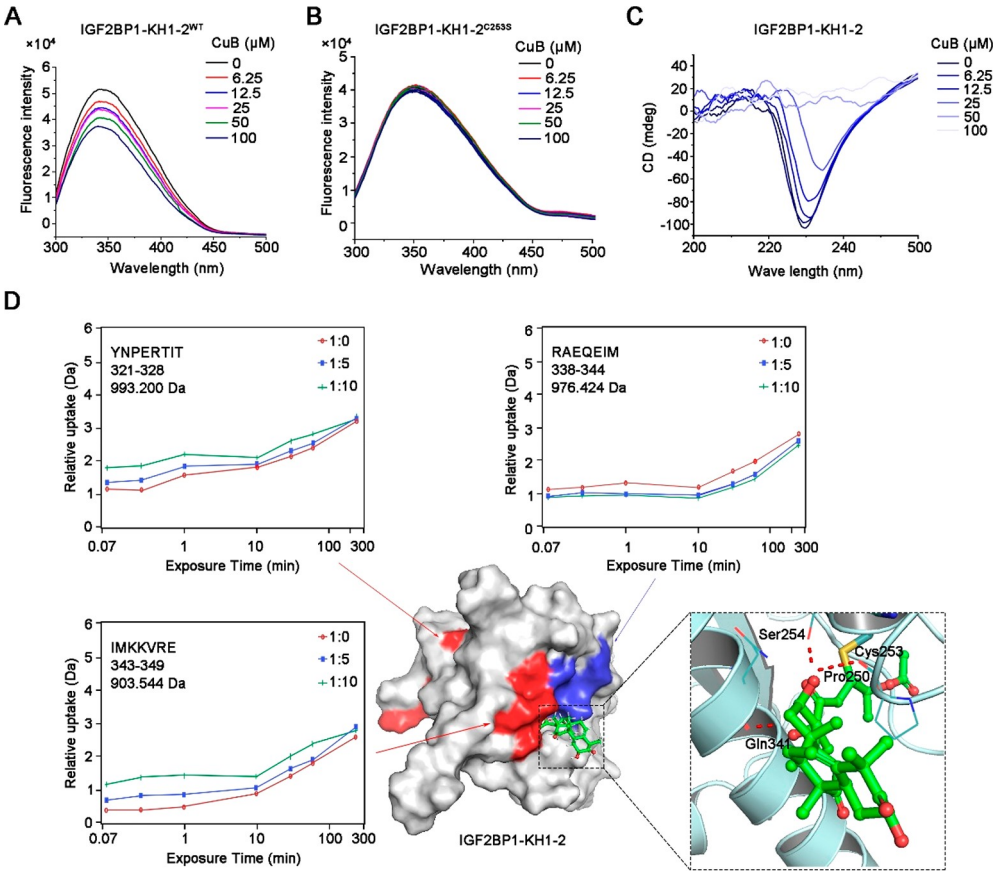

Figure 4. CuB allosterically regulates the IGF2BP1 conformation. (A) Fluorescence spectroscopy analysis for CuB-mediated recombinant IGF2BP1-KH1−2 conformational change. (B) Cys253 mutation blocked the conformation change of recombinant IGF2BP1-KH1−2. (C) CD spectra analysis for CuB-mediated recombinant IGF2BP1-KH1−2 conformational change. (D) CuB allosterically regulated the recombinant IGF2BP1-KH1−2 conformation by HDX-MS. Deuterium uptake plots of these peptides upon addition of CuB were presented, and the molar ratios of IGF2BP1-KH1−2 to CuB were presented in the top right of the deuterium uptake plots. Peptides with a higher or lower deuterium uptake ratio after a CuB treatment were highlighted in red or blue colors on an X-ray crystal structure of IGF2BP1-KH1−2 (PDB: 6QEY), respectively.

fluorescent labeling (Figure S2F−I). We found that Biotin-CuB retained the robust inhibition of Huh7 cell viability, indicating that the biotin modification did not affect CuB antitumor activity (Figure S2J). A pull-down assay demonstrated that Biotin-CuB could effectively capture native IGF2BP1 from cell lysates (Figure 2G). Further immunofluorescence staining showed obvious overlap (yellow) between the IGF2BP1 (red) and Biotin-CuB (green) signals, indicating a direct interaction of CuB-IGF2BP1 in cells (Figure 2H). In addition, IGF2BP1 knockdown markedly abolished CuB-mediated inhibition of tumor cell proliferation both in vitro and in vivo (Figures 2I−K and S2K). We also evaluated the proteome-wide selectivity of IGF2BP1 with CuB in cells. A pull-down assay coupled with silver staining and a liquid chromatography-mass spectrometry (LC-MS) analysis demonstrated that IGF2BP1 served as a specific CuB-binding protein in the proteome-wide scale (Figure S2L, Table S1). Collectively, these findings suggested that CuB directly targeted IGF2BP1 in Huh7 cells.

Cys253 Serves as a Covalent Modification Site of CuB. To investigate the residues involved in CuB interaction with IGF2BP1, we first tested whether CuB could covalently bind with IGF2BP1. Western blots revealed that IGF2BP1 was pulled down by Biotin-CuB bound beads, which was abolished by cotreatment with free CuB (Figure 3A). However, when IGF2BP1 was preincubated with Biotin-CuB beads, post-treatment with an excess of free CuB did not affect IGF2BP1 binding to the beads, indicating the formation of covalent bonds between CuB and IGF2BP1 protein (Figure 3B). Considering that CuB contains an α,β-unsaturated carbonyl group, which potentially reacts with the thiol of cysteine on IGF2BP1, we next incubated IGF2BP1 with Biotin-CuB beads in the presence or absence of β-mercaptoethanol (BME)/dithiothreitol (DTT) to investigate whether there was a competitive binding with IGF2BP1 via thiols. As shown in Figure 3C, BME or DTT significantly attenuated IGF2BP1 binding to Biotin-CuB beads, which suggested that CuB could covalently bind to the thiols of cysteine.

We further wondered which domain of IGF2BP1 interacted with CuB. IGF2BP1 consists of six functional domains, including RRM1−2 and KH1−4 (Figure 3D). In order to identify the specific CuB binding site on IGF2BP1, we performed pull-down assays with IGF2BP1 variants harboring truncations of the two RRM or four KH domains. These results revealed that IGF2BP1 could still interact with Biotin-CuB beads despite deletion of both N-terminal RRM domains. However, deletion of the C-terminal KH domains abolished its binding with the Biotin-CuB beads (Figure 3E). Successive truncations showed that the KH1−2 domains, but not KH3−4 domains, were indispensable for interaction with CuB (Figure 3F).

https://doi.org/10.1021/acscentsci.2c00107
ACS Cent. Sci. 2022, 8, 1102−1115

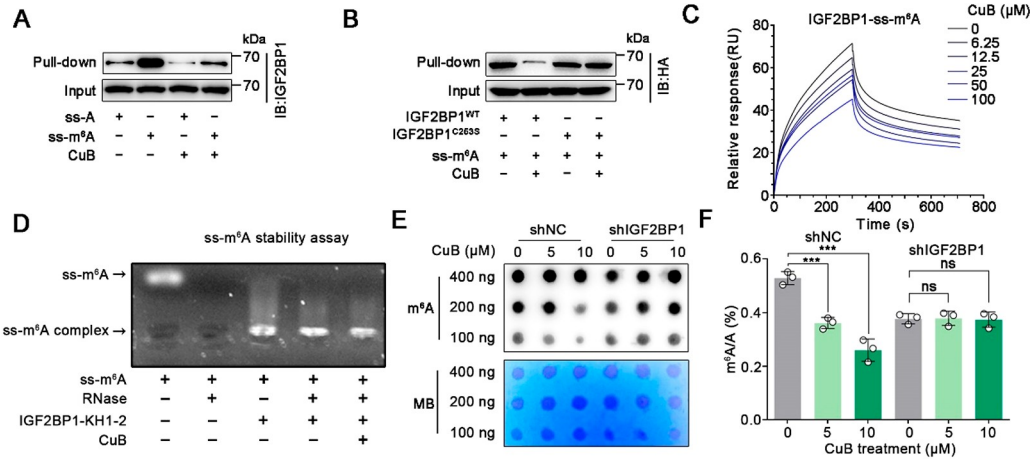

Figure 5. CuB inhibits IGF2BP1 binding to mRNA targets in an m^{6}A-dependent manner. (A) CuB inhibited IGF2BP1 interaction with the ss-m^{6}A probe using a pull-down assay. (B) Cys253 mutation abolished the inhibitory effect of CuB on IGF2BP1 interaction with ss-m^{6}A. (C) CuB attenuated IGF2BP1 interaction with ss-m^{6}A in the presence of CuB for the competitive binding by an SPR analysis. (D) CuB blocked the protection effect of IGF2BP1 on the ss-m^{6}A probe by agarose gel electrophoresis in the presence of RNase. (E) Determination of global m^{6}A abundance in Huh7 cells upon CuB treatment for 24 h via a dot blot assay. Methylene blue represents the loading control of RNA samples. (F) Quantitation of the percentage of m^{6}A/A in mRNA by LC-MS/MS in Huh7 cells treated with CuB for 24 h. Data are shown as mean ± SD. ***P < 0.001 vs Ctrl group. ns, not significant.

A basic local alignment search tool (BLAST) analysis using the IGF2BP1-KH1−2 protein sequence as a query revealed four cysteine residues. To determine which cysteine residue was attacked by CuB, we incubated recombinant IGF2BP1 with or without CuB and then conducted an LC-MS/MS analysis to determine which tryptic peptides contain a CuB modification. This analysis identified a peptide with a calculated mass of 2347.0571 Da, which was 558.3156 Da larger than the Cys253-containing peptide ENAGAA-EKAISVHSTPEGCSSACK (2905.3727 Da) (Figure 3G, Table S2). This mass difference of 558.3156 Da exactly matched the molecular weight of the CuB. The mass shift was not observed in fragment ion y^{2+}, indicating that the cysteine in this peptide (Cys253 in IGF2BP1) was covalently modified by CuB. To test whether this residue was indeed the relevant site for CuB binding, we next introduced nonsynonymous mutations that converted four cysteine residues to serines in the KH1−2 domains. Pull-down assays further supported that CuB covalently modified Cys253 but not other cysteines including Cys257, Cys336, and Cys337 (Figure 3H). Moreover, we re-expressed IGF2BP1^{WT} or IGF2BP1^{C253S} mutant in IGF2BP1 knockdown Huh7 cells and then examined the antiproliferative effect of CuB. Interestingly, IGF2BP1^{WT}, but not IGF2BP1 ^{C253S} variant, restored the CuB-mediated inhibition of Huh7 cell proliferation with IC_{50} 3.1 μM for 48 h (Figure S3A). Additionally, the CuB-EGCSS (a synthetic peptide) complex formation was also accurately confirmed and quantified using both LC-MS and NMR analysis (Figure S3B−F). Together, these results suggested that cysteine could form a covalent adduct on an α,β-unsaturated carbonyl group of CuB via a Michael addition.

Finally, to determine whether other noncovalent interactions participated in IGF2BP1-CuB complex formation, we performed molecular docking simulations using Maestro (Schrödinger, ver. 9.0). We found that the stereo conformation of CuB fitted well with the binding site around reactive Cys253 and that 21-hydroxyl and 22-keto groups of CuB could form additional hydrogen bonds with Gln 341 and Ser254 residues, respectively (Figure 3I). Collectively, these results indicated that CuB covalently bound to the Cys253 residue of IGF2BP1 via a Michael addition reaction.

CuB Allosterically Regulates IGF2BP1 Conformation Via Cys253. Allosteric effects represent a crucial mechanism for regulating protein function.[30] Since the IGF2BP1-KH1−2 domains formed a stable monomeric structural unit for m^{6}A RNA binding, we then speculated that CuB could affect the IGF2BP1 conformation due to their high modification efficiency. To this end, we quantified tryptophan fluorescence in recombinant IGF2BP1-KH1−2^{WT} or IGF2BP1-KH1−2^{C253S}. We found that CuB caused a concentration-dependent decrease of the tryptophan fluorescence intensity, but not in the C253S variant, implying that CuB may induce conformational changes by binding with Cys253 in IGF2BP1-KH1−2 (Figure 4A,B). We then used circular dichroism (CD) spectroscopy to determine the secondary structure of IGF2BP1-KH1−2 and found the typical α-helix-rich protein characteristics reported in previous studies.[25] Upon exposure of IGF2BP1-KH1−2 to CuB, we observed a progressive decrease in the molar ellipticity values at 222 nm, suggesting a concentration-dependent reduction in protein helicity (Figure 4C). These findings revealed that complex formation with CuB likely induced conformational changes in IGF2BP1-KH1−2.

To explore the allosteric mechanism in fine detail, we performed hydrogen−deuterium exchange mass spectrometry (HDX-MS). IGF2BP1-KH1−2 is comprised of two domains containing six α-helices (α1-α3) with short loops between them. The HDX-MS profile of IGF2BP1-KH1−2 revealed that the amino acids in loops exposed to buffer had a higher deuterium uptake than buried regions with a well-ordered α-helical secondary structure. Moreover, CuB increased the hydrogen/deuterium exchange levels of two specific peptides, namely, YNPERTIT in the β3-strand and IMKKVRE in the α3-helix of the KH2 domain, and slightly decreased the hydrogen/deuterium exchange level of the RAEQEIM peptide in KH-2 α3-helix, which was essential for the stability of the monomeric units for RNA binding (Figures 4D and S4).[25] The decrease in the hydrogen/deuterium exchange rate at the α3-helix revealed that CuB was embedded in the KH2 domain,

https://doi.org/10.1021/acscentsci.2c00107
ACS Cent. Sci. 2022, 8, 1102−1115

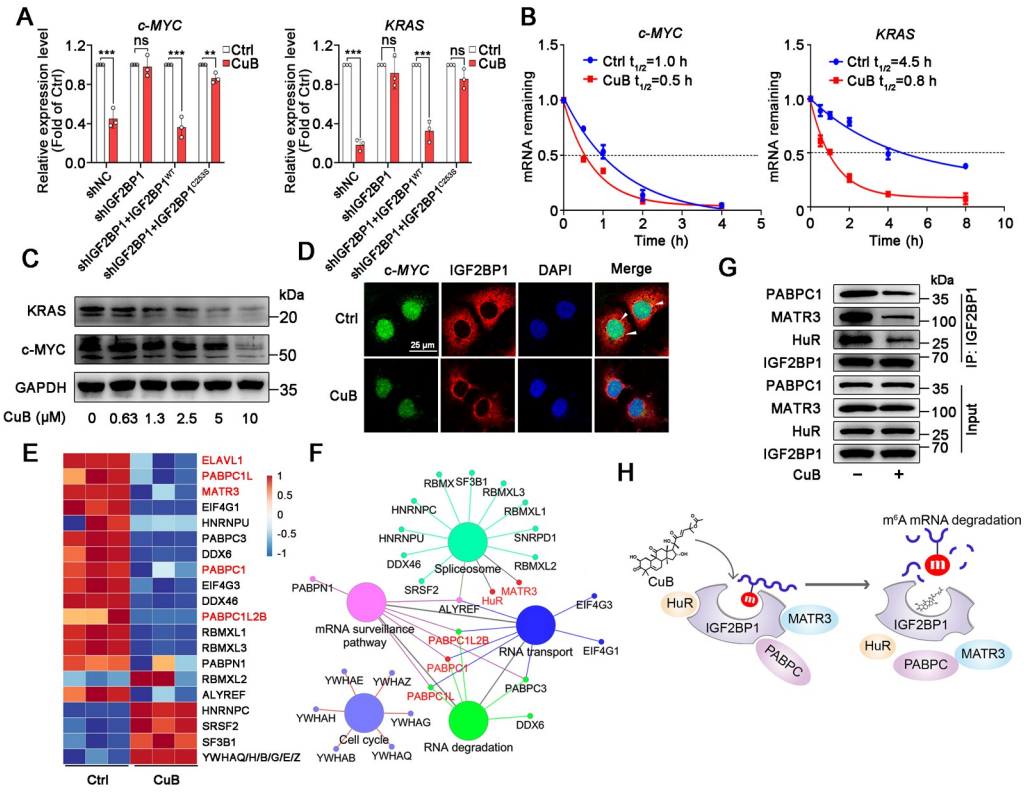

Figure 6. CuB reduces the m^{6}A mRNA stability via directly targeting IGF2BP1. (A) Effects of CuB treatment of 24 h on c-*MYC* and *KRAS* mRNA expression in Huh7 cells by RT-PCR. (B) *KRAS* and c-*MYC* mRNA stability changes in Huh7 cells upon CuB treatment. (C) Effects of CuB treatment of 24 h on KRAS and c-MYC expression levels in Huh7 cells by a western blot. (D) Fluorescence in situ hybridization images of labeled c-*MYC* RNA upon CuB treatment for 24 h in Huh7 cells. White arrows indicate overlapped signals. (E) Heat map of differentially regulated proteins involved in significantly canonical pathways after treatment with CuB for 12 h in Huh7 cells. (F) KEGG pathway enrichment analysis for the significantly differentially regulated protein predicted the significantly canonical pathways. (G) HuR, MATR3, and PABPC1 interaction with IGF2BP1 was inhibited by CuB in Huh7 cells after 12 h of treatment, respectively. (H) Schematic of IGF2BP1-m^{6}A mRNA interaction and partners regulation in response to CuB treatment. Data are shown as mean ± SD. $^{**}P < 0.01$ and $^{***}P < 0.001$ vs Ctrl group. ns, not significant.

thereby impairing IGF2BP1 binding to its targets. Together, these results confirmed that CuB could act as an allosteric regulator of IGF2BP1.

CuB Suppresses IGF2BP1 Recognition of m^{6}A mRNA Targets. To investigate whether allosteric regulation of IGF2BP1 by CuB had an impact on m^{6}A targets, we conducted RNA pull-down assays using ss-m^{6}A and ss-A. Notably, the data supported that IGF2BP1 preferentially bound to the ss-m^{6}A probe, which was reversed in the presence of CuB (Figure 5A). However, the specific interaction between methylated RNA bait and IGF2BP1 could not be disturbed by the CuB treatment in its mutant, suggesting the inhibition effect of CuB was Cys253-dependent (Figure 5B). Additionally, these observations were confirmed by a quantitative SPR analysis in which CuB specifically disrupted the IGF2BP1 interaction with the ss-m^{6}A probe (Figure 5C). Collectively, these data implied that CuB may block IGF2BP1 binding to mRNAs.

We then hypothesized that CuB could reduce IGF2BP1 target stability by disrupting their interaction. To this end, we examined ss-m^{6}A concentrations in the presence of IGF2BP1 with or without CuB. As shown in Figure 5D, IGF2BP1-KH1−2 protein significantly limited ss-m^{6}A probe degradation upon RNase, which was substantially abolished by CuB. These results suggested that CuB could reduce the stability of m^{6}A mRNA via an IGF2BP1-dependent manner. Furthermore, in m^{6}A dot blot assays, we found that a CuB treatment resulted in a substantial decrease in transcriptome-wide m^{6}A abundance in Huh7 cells, which was reversed in IGF2BP1 knockdown cells (Figure 5E). LC-MS/MS quantification further confirmed the decrease in m^{6}A mRNA after exposure to CuB (Figure 5F).

We next sought to confirm the inhibitory effect of CuB on IGF2BP1-mediated mRNA stabilization. We found that CuB significantly decreased the transcript abundance of *c-MYC*, *KRAS*, *MARCKSL1*, and *FSCN1* in Huh7 cells, which was abolished in IGF2BP1 knockdown Huh7 cells. In addition, CuB-mediated degradation effects were markedly reversed by re-expressed IGF2BP1^{WT} but not IGF2BP1^{C253S} mutant (Figures 6A and S5A). Thus, these observations supported that CuB regulated mRNA stability in an IGF2BP1-dependent manner particularly via the Cys253 site.

Then, we observed that CuB dramatically decreased the half-life of both c-*MYC* and *KRAS* mRNAs (Figure 6B). Western blots supported the inhibitory effects of CuB on c-MYC and KRAS accumulation at the protein level (Figure 6C). Moreover, RNA-fluorescence in situ hybridization (RNA-FISH) assays also confirmed that CuB inhibited IGF2BP1 colocalization with c-*MYC* mRNA (Figure 6D).

Subsequently, we performed coimmunoprecipitation (Co-IP) experiments to dissect the effect of CuB on IGF2BP1 partners. The protein levels of these participants were normalized by IGF2BP1 and then compared with a control (Ctrl) group to give the differentially regulated proteins (DRPs). Protein identification of the Huh7 cell lysates against the Thermo Proteome Discoverer database showed more than

https://doi.org/10.1021/acscentsci.2c00107
ACS Cent. Sci. 2022, 8, 1102−1115

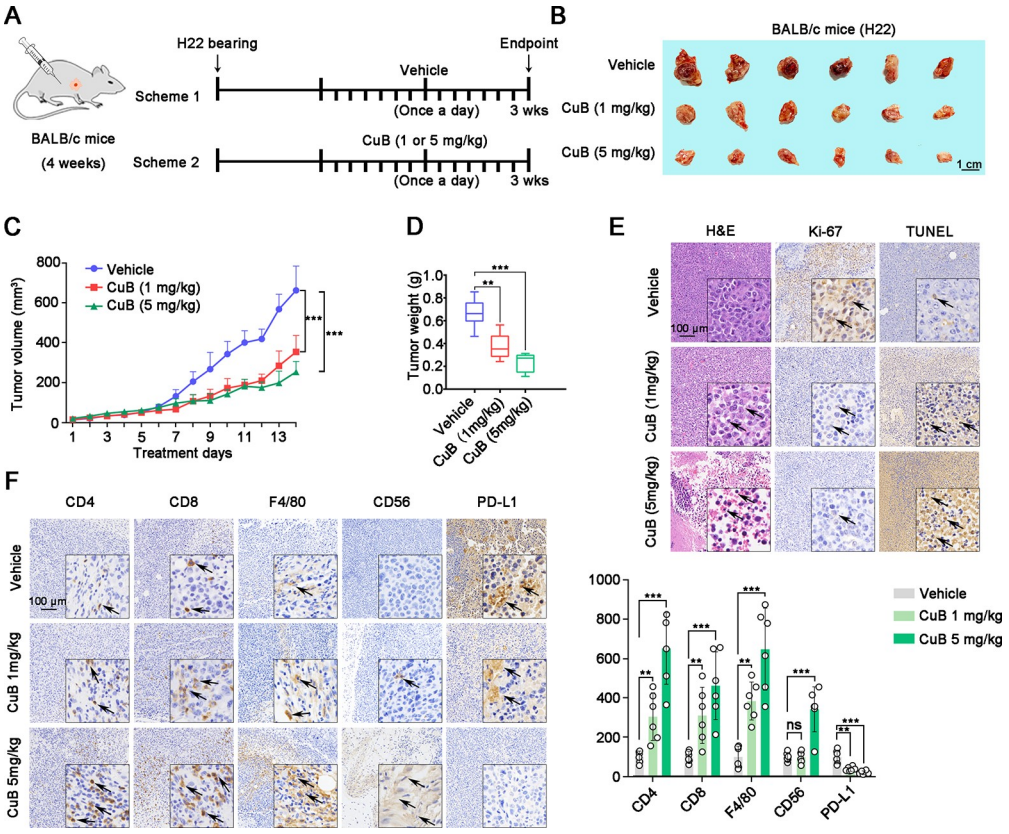

Figure 7. CuB exerts antitumor effects via activation of the TIME. (A) Schematic diagram of the CuB administration procedure in the established H22 tumor-bearing mice. BALB/c mice bearing an H22 xenograft were given CuB (1 or 5 mg/kg) by intraperitoneal injection per day for a 14 d treatment. (B) Images of excised tumors after the CuB treatment in BALB/c mice bearing H22 xenografts (n = 6). (C) The dynamic change of tumor volume in subcutaneous models was shown. (D) The weight of subcutaneous xenograft tumors (n = 6). (E) Representative histological analysis of tumor specimen stained by H&E, Ki-67, and TUNEL (scale bars = 100 μm). (F) Representative images of IHC staining for CD4, CD8, F4/80, CD56, and PD-L1 in tumor tissues. Black arrows indicate positive staining cells. Quantification of IHC staining is shown (n = 6). Data shown as mean ± SD. $^{**}P < 0.01$ and $^{***}P < 0.001$ vs vehicle group.

250 candidates were identified, and 60 DRPs with a $|\log_2\text{foldchange}| > 1$ was examined for enrichment in a Kyoto Encyclopedia of Genes and Genomes (KEGG) pathway analysis (Table S3). The global pathway networks were mainly involved in the cell cycle, spliceosome, mRNA surveillance pathway, RNA transport, or RNA degradation (Figure 6E,F). Notably, CuB negatively regulated the accumulation of previously reported mRNA stabilizers HuR, MATR3, and PABPC1,[13] which were enriched in these pathways. Western blots confirmed that CuB treatment remarkably impaired IGF2BP1 interaction with these partners, but without obvious changes in their protein expression levels (Figures 6G and S5B, Table S4). Collectively, these findings suggested that CuB effectively reduced m^{6}A RNA stability in an IGF2BP1-dependent manner (Figure 6H).

Additionally, to investigate the role of IGF2BP1 as an effector of CuB, we compared the transcriptome changes by a CuB treatment or IGF2BP1 knockdown in Huh7 cells. We observed 1472 genes with altered expression in wild-type cells treated with CuB and 1375 genes with altered expression after IGF2BP1 knockdown. Given that IGF2BP1 was typically associated with mRNA stability and translation, we then focused on the genes that were downregulated by a CuB treatment. As a result, 846 of 1472 downregulated genes (57.5%) by CuB were also observed in the IGF2BP1 knockdown cells (Figure S6A, Table S5). These results indicated that the CuB treatment phenocopied the genetic IGF2BP1 knockdown on the gene expression pattern. Furthermore, we performed a gene ontology (GO) enrichment analysis, including cellular component (CC), biological process (BP), and molecular function (MF), to elucidate the potential functions of these downregulated differentially expressed genes. As shown in Figure S6B, many of these genes were involved in the regulation of transcription, apoptosis process, cell cycle, and inflammatory response. The global pathway network depicting the KEGG pathway analysis were mainly enriched in signaling pathways mediated by cytokines, such as tumor necrosis factor (TNF), toll-like receptor, and NF-κB (Figure S6C). Together, these findings supported the conclusion that CuB promoted IGF2BP1-dependent target mRNA degradation to induce tumor cell apoptosis.

CuB Exerts Antitumor Effects Via Recruiting Immune Cells and Blocking PD-L1 Expression. To determine whether CuB could inhibit tumor growth in vivo, we examined its effects on H22-derived tumors in BALB/c mice (Figure 7A). Following the intraperitoneal injection of CuB (1 or 5 mg/kg) once daily for 14 d, in agreement with our above results, CuB treatment led to substantially reduced tumor volume and weight in xenograft model mice compared with a control group with no obvious change in body and organ weight (Figures 7B–D and S7A,B). A pathological examination by H&E staining showed that xenograft tumor cells were loosely packed with small nuclei compared with a control group (Figure 7E). In Ki-67 and TUNEL IHC assays, CuB

https://doi.org/10.1021/acscentsci.2c00107
ACS Cent. Sci. 2022, 8, 1102−1115

strongly suppressed the expression of Ki-67 positive cells and induced apoptosis of HCC cells (Figure 7E), indicating that CuB triggered an obvious antitumor effect.

Next, we performed IHC staining to evaluate the proportions of tumor-infiltrating immune cells in HCC. As expected, we found obvious elevations in the number of $CD4^+$ and $CD8^+$ T cells in CuB-treated mice, demonstrating that CuB could increase intratumoral T cell infiltration (Figure 7F). As a crucial T cell immune checkpoint protein, we then investigated whether CuB exposure affected PD-L1 expression. IHC assays revealed that CuB dramatically attenuated the cell surface PD-L1 expression in H22 xenograft mice in vivo (Figure 7F). Taken together, these results suggested that CuB triggered antitumor immunity by synchronously recruiting immune cells and blocking immunosuppressive PD-L1 expression.

DISCUSSION

Previous investigations identified BTYNB as the first small-molecule inhibitor of IGF2BP1 binding to target mRNAs that showed therapeutic potential by inhibition of IGF2BP1-positive cancer cell proliferation.[31,32] However, it remained unclear whether BTYNB could directly bind with IGF2BP1. In this study, we discovered that CuB, a tetracyclic triterpenoid, could directly target IGF2BP1, resulting in HCC cell apoptosis and increased intratumoral T cell infiltration in an m^6A-dependent manner. In particular, we identified Cys253, which represented a unique druggable active site in the KH1−2 domain of IGF2BP1.

Generally, IGF2BP1 carries six conserved RNA-binding domains, including four KH domains and two RRMs. It is noteworthy that the KH1−2 domain plays an essential role in stabilizing IGF2BP1-RNA complexes via mediating IGF2BP1 binding to cis-elements in the 3′-UTR of the target gene mRNA.[25] CuB could allosterically regulate of the KH1−2 domain to prevent IGF2BP1-dependent m^6A mRNA binding by increasing anisotropy at the IGF2BP1 protein surface. Therefore, we provided, to our knowledge, the first demonstration of a small-molecule-mediated allosteric negative regulatory mechanism controlling the IGF2BP1 stabilization of m^6A-modified mRNAs.

Covalent inhibitors are currently recognized as a major resource for drug discovery and therapeutic development.[33,34] Here, we found that a double bond conjugated with a carbonyl group in CuB could be attacked by Cys253 of IGF2BP1 through a thiol-Michael addition reaction, resulting in an irreversible covalent product and allosteric change of IGF2BP1. Interestingly, we incubated CuB with mercapto-rich reagents (e.g., cysteine or 2-mercaptoethanol) in an aqueous environment but did not detect the expected addition products. Instead, our result suggested that the attack of CuB by Cys253 may be governed by the local chemical environment. First, the IGF2BP1 ligand-binding domain provided a high-affinity target-binding cavity-like structure via hydrogen bonding and electrostatic attraction, further prolonging the CuB residence time at the reaction site and increasing the collision probabilities to reaction rate. In addition, the active pocket in IGF2BP1 may also provide effective support for unstable high-energy reaction intermediates, although further experimental evidence is needed to support this hypothesis.

Immunotherapy can help to strengthen or restore the immune system ability to fight cancer. c-MYC, overexpressed in many human cancers, is a transcription factor that regulates the expression of numerous genes involved in cell proliferation, growth, differentiation, and apoptosis.[35,36] c-MYC is considered as a central regulator of PD-L1 expression by directly binding to the PD-L1 promoter in various cancer types.[37,38] Thus, silencing c-MYC expression leads to tumor regression through remodeling of the TIME in multiple tumor models. In addition, c-MYC knockdown can further enhance the immune response by promoting immune cell tumor infiltration. Therefore, therapies suppressing c-MYC expression could restore the anticancer immune response. Our finding highlighted the potential effectiveness of strategies targeting IGF2BP1 with a small molecule to reshape TIME in an m^6A-dependent manner.

Collectively, this study revealed IGF2BP1 as a novel allosteric target for cancer therapeutics via regulating TIME. Moreover, CuB may serve as a promising drug candidate for developing a mechanistic understanding of IGF2BP1 biology in m^6A regulation.

MATERIALS AND METHODS

Chemicals and Reagents. Cucurbitacin B ($C_{32}H_{46}O_8$) was purchased from Baoji Herbest Biotech, and the purity was determined to be 99.35% based on high-performance liquid chromatography (HPLC). Biotin-linker ($C_{17}H_{28}N_2O_5S$) was obtained by Wuxi App Tech. Fetal bovine serum (FBS) was from PAN-Biotech. Antibiotics and trypsin were from Macgene. Deionized water was obtained from a Milli-Q system. Lipofectamine RNA iMAX and Lipofectamine 2000 were obtained from Thermo Fisher Scientific. Pronase was from Roche Diagnostics GmbH. K_i-67, CD4, CD8, CD56, F4/80, c-MYC, KRAS, m^6A, PABPC1, MATR3, HuR, and HA antibodies were from Cell Signaling Technology. Antibodies against IGF2BP1, PD-L1, and HRP-conjugated goat antirabbit IgG were supplied by Proteintech Group. An RNA FISH kit was obtained from GenePharma. ss-m^6A, ss-A, and EGGCS peptide were synthesized by GenScript. The IGF2BP1 shRNA plasmid for mouse was purchased from Santa Cruz Biotechnology. The primers were designed and synthesized by Shanghai Generay Biotech.

Synthesis of Biotin-CuB Probe. CuB (558.7 mg, 1 mmol, 1 equiv), Biotin-linker (372.5 mg, 1 mmol, 1 equiv), *N*,*N*′-dicyclohexylcarbodiimide (DCC) (309.1 mg, 1.5 mmol, 1.5 equiv), and 4-dimethylaminopyridine (DMAP) (183.3 mg, 1.5 mmol, 1.5 equiv) were dissolved with 5 mL of dichloromethane solvent. The reaction mixture was stirred at room temperature overnight, and then the reaction was terminated by adding onefold deionized water. The mixture was extracted with 15 mL of ethyl acetate three times. The organic extracts were concentrated to dryness under vacuum. The residue was prepared by semipreparative HPLC eluting with 80% (v/v) acetonitrile (ACN)/H_2O to yield Biotin-CuB (400.5 mg, 43.8% yield). The chemical structure of Biotin-CuB was determined by NMR.

Bioinformatics Analysis of Liver Hepatocellular Carcinoma in TCGA Database. The Cancer Genome Atlas is a data resource for cancer bioinformatics analysis. UALCAN (http://ualcan.path.uab.edu) and GEPIA (http://gepia.cancer-pku.cn) are two web-based tools for analyzing TCGA clinical data to evaluate the association of gene expression and patient survival. The UALCAN Web site was applied to analyze the expression difference of target genes based on individual cancer stages. A five-year survival analysis was

https://doi.org/10.1021/acscentsci.2c00107
ACS Cent. Sci. 2022, 8, 1102−1115

conducted on genes with high or low expression using the GEPIA Web site.

Immunohistochemical Staining for Tissue Microarray Analysis. The tissue chip HLivH180Su18, which contained samples form 90 cases of human hepatocellular carcinoma, was purchased from Shanghai Outdo Biotech. Informed consent was obtained from all subjects in accordance with the protocol approved by the individual institutional Ethics Committees. Sections were semiquantitatively scored for the IGF2BP1 staining patterns as follows: the staining intensity was quantified as 0 (negative), 1+ (weak), 2+ (intermediate), or 3+ (strong).

High-Throughput SPR Screening for Small-Molecule Inhibitors. SPR screening was performed using a Biacore 8k (GE healthcare) instrument at 25 °C. A CM5 sensor chip was active by using sulpho-*N*-hydroxysuccinimide (NHS)/1-ethyl-3-(3-dimethylaminopropyl) carbodiimide (EDC) chemistry. The chip was subsequently immobilized with the streptavidin at a concentration of 500 μg/mL in sodium acetate, pH 4.5, and then immobilized with a biotin-modified ss-m^{6}A probe at 10 ng/mL. Various concentrations of recombinant IGF2BP1 were injected for method validation at a flow rate of 30 μL/min in PBS-P (10 mM phosphate buffer with 2.7 mM KCl and 137 mM NaCl, 0.05% Surfactant P20, and 5% dimethyl sulfoxide (DMSO)) running buffer. The Medicinal Natural Products Library contains 889 compounds that were dissolved in DMSO and further diluted with PBS-P buffer and analyzed at a final concentration of 20 μM (5% DMSO). The results were analyzed with the Biacore evaluation sofeware (8k, ver. 2.0). The interaction between CuB and IGF2BP1 was fitted to the steady-state affinity model to obtain results.

Mice and Cell Lines. Male BALB/c mice (four weeks) were purchased from the Department of Laboratory Animal Science of Peking University Health Science Center and maintained under specific pathogen-free (SPF) conditions in a controlled environment of 22−22 °C approved by the Ethical Guidelines of EIACUC-PKU (A2021230). Mice were kept for 48 h to acclimatize to the environment and fasted overnight before treatment.

Human hepatoma Huh7, HEK293T, and mouse H22 cells were obtained from Peking Union Medical College, Cell Bank. Cells were routinely maintained in high-glucose Dulbecco's Modified Eagle's Medium (DMEM) supplemented with 10% FBS, 100 U/mL penicillin, and 100 μg/mL streptomycin at 37 °C in a 5% CO_2 humidified incubator.

Cellular Target Identification of CuB. Huh7 cell lysates were incubated with vehicle or CuB beads in the absence or presence of CuB overnight at 4 °C. The beads were subsequently washed six times with PBS to remove the nonspecific proteins. The beads-binding proteins were separated by sodium dodecyl sulfate polyacrylamide gel electrophoresis (SDS-PAGE) and detected by a silver staining assay. The protein bands with an obvious difference upon CuB treatment were excised, trypsin-digested, and then analyzed by LC-MS/MS. The trypsin-digested peptides were filtered through the 0.22 μm micropore membrane and then subjected to liquid chromatography coupled with an LTQ Velos pro mass spectrometer (Thermo Scientific). The captrap peptide column was used to load the peptide solution, and then the analytes were separated by an RP-C18Q column (100 μm id ×15 cm) with the column oven temperature of 35 °C.

Identification of CuB-Binding Site on IGF2BP1. Recombinant IGF2BP1 protein was incubated with CuB for 48 h at a concentration of 0.5 mM, and the mixtures were subjected to SDS-PAGE and stained with coomassie blue. The band corresponding to IGF2BP1 was excised and digested in gel with trypsin. Extracted peptides were separated using an EASY-LC system and conducted by nano-liquid chromatography linear trap quadrupole mass spectrometry (LC-LTQ-MS). The mixtures were autosampled directly, bound onto a trapping column, and eluted with the following gradient: 2%−40% B for 70 min; 40%−95% B for 5 min; 95% B for 20 min (solvent A: 0.1% formic acid in H_2O, solvent B: 0.1% formic acid in ACN). The eluent was introduced to the mass spectrometer at a flow rate of 300 μL/min. Full scan MS spectra (m/z 350−2000) were acquired in the Orbitrap analyzer with a resolution of 60 000. The top 15 most abundant precursor ions from each MS scan with charge states of at least 2 were selected for MS/MS scans in the linear ion trap analyzer with a collision-induced dissociation (CID) of 35% collision energy. MS data were analyzed with Proteome Discoverer (1.4) software with the SEQUEST search engine (Thermo Fisher Scientific) using the following criteria: taxonomy, human; enzyme, trypsin; missed cleavage sites, 2; variable modifications, methionine oxidation (+15.9950 Da), cysteine carbamidomethylation (+57.0210 Da), cysteine binding with IGF2BP1 (+558.3193 Da); precursor mass tolerance as 10 ppm, fragment mass tolerance as 0.6 Da; and the false discovery rate (FDR) at 0.01.

Western Blot. Total proteins were extracted from the cells by radioimmunoprecipitation assay (RIPA) buffer containing protease inhibitors (Macgene) and centrifuged at 12 000 rpm for 10 min at 4 °C. The total protein concentration was determined by bicinchoninic acid (BCA) protein assay reagent (TransGen). Protein samples were transferred to a poly-(vinylidene difluoride) (PVDF) membrane (Millipore) after being separated by SDS-PAGE. Membranes were blocked with 5% skim milk at 25 °C for 30 min and then incubated with primary antibodies overnight at 4 °C. Subsequently, membranes were incubated with horseradish peroxidase (HRP)-conjugated antirabbit or antimouse IgG secondary antibody for 1 h at room temperature. The membranes were analyzed by a Tanon-5200 Multi Gel Imaging Analysis System (Tanon) and quantified by ImageJ software (ver. 1.8.0).

Molecular Docking. An X-ray structure of human IGF2BP1-KH1−2 (PDB: 6QEY) was downloaded from the Protein Data Bank. Molecular docking of CuB to IGF2BP1-KH1−2 was performed using the DS-CDOCKER protocol implemented through the graphical user interface of the Discovery Studio software (ver. 2020). The three-dimensional structure of CuB was constructed using Chem3D Ultra 12.0 software (Chemical Structure Drawing Standard, CambridgeSoft 14.0) and was energetically minimized using the MMFF94 force field with 5000 iterations and a minimum root-mean-squared (RMS) gradient of 0.10.

CETSA. The cellular target identification of CuB was performed using CETSA as previously described.[39] Briefly, the cells were treated with or without CuB for 2 h and then heated individually at different temperatures (37−64 °C) for 3 min followed by cooling on ice. The cell lysates were obtained by five repeated freeze−thaw cycles in liquid nitrogen. The soluble lysates were centrifuged, and supernatants were detected by a western blot.

DARTS Assay. A DARTS assay was conducted as previously described.[39] Briefly, the cell lysates were diluted (1:10) with TNC buffer (50 mM Tris-HCl, 50 mM NaCl, 10

https://doi.org/10.1021/acscentsci.2c00107
ACS Cent. Sci. 2022, 8, 1102−1115

mM $CaCl_2$) and then treated with indicated concentrations of CuB or DMSO as a control. After incubation for 30 min at room temperature, 5 μg/mL Pronase was added, and the mixture was incubated further for 30 min. Reactions were stopped by being mixed with the loading buffer and then were analyzed by a western blot.

Recombinant IGF2BP1 Expression and Purification. The DNA sequences encoding IGF2BP1 and IGF2BP1-KH1−2 were cloned into the *Kpn*I/*Hin*dIII restriction sites of the modified pCold-SUMO vector with His-tag. The Artic Express *Escherichia coli* cells were transformed with the plasmid. This bacterial preculture was poured into 2 L of the same medium and incubated at 37 °C and 160 rpm until OD600 reached 0.6. Then, cells were induced using isopropyl β-D-1-thiogalactopyranoside (IPTG) at a final concentration of 1 mM and incubated at 12 °C for 72 h. Cells were harvested, lysed, and clarified by centrifugation at 12 000 rpm at 4 °C. The supernatant was loaded into a 5 mL His column equilibrated in lysis buffer. Nonspecific binding protein was washed with binding buffer, and recombinant IGF2BP1 was collected with elution buffer (same as the lysis buffer but with 250 mM imidazole). The concentration of IGF2BP1 was quantified by the BCA protein assay reagent.

Co-Immunoprecipitation (Co-IP) Assay. The cells were collected and incubated with immunoprecipitation (IP) buffer (Beyotime) at 4 °C for 20 min. The lysates were then centrifuged at 12 000*g* at 4 °C for 20 min. The supernatants were collected and incubated with IGF2BP1 antibody for 1 h. The immunocomplexes were then incubated with protein A/G-agarose and agitated on ice for 4 h. The beads were subsequently washed, trypsin-digested, and then analyzed by nano-LC-LTQ-MS with the following gradient: 2%−40% B for 70 min; 40%−95% B for 5 min; 95% B for 20 min (solvent A: 0.1% formic acid in H_2O, solvent B: 0.1% formic acid in ACN).

Data acquisition was conducted using a data-dependent strategy on a high-resolution LTQ-Orbitrap Velos Pro hybrid mass spectrometer (Thermo Fisher Scientific). The Orbitrap mass spectrometer was equipped with a nanoelectrospray ion source with an ion spray voltage of 1.8 kV and an Orbitrap analyzer with of resolution of 60 000 (full width at half-maximum). Collision energy for CID was set at 25 eV. The raw MS/MS data were then processed, and the protein identification was searched for in the Thermo Proteome Discoverer (v.1.4.1.14) software. Data were expressed from three individual experiments. The signaling pathway enrichment analysis was performed using the KEGG database from the ClueGO program, a plug-in Cytoscape software (v.3.4.0).

Dot Blot Analysis. To determine global m^6A abundance, dot blot assays were employed with poly(A)$^+$ RNA. Briefly, the indicated amount of RNA was denatured in a threefold volume of RNA incubation buffer (65.7% fomamide, 7.77% formaldehyde, and 1.33× 3-(*N*-morpholino)propanesulfonic acid (MOPS)) at 65 °C for 5 min. Then 100 μL of chilled 20× saline−sodium citrate (SSC) buffer was added and mixed well before samples were loaded onto the Amersham Hybond-N+ membrane with a Bio-Dot Apparatus. After it was allowed to cross-link under 254 nm UV for 5 min, the membrane was stained with methyl blue, and the image was captured. The membrane was then washed with PBST buffer, blocked with 5% nonfat milk, and incubated with rabbit anti-m^6A antibody overnight at 4 °C. After it was washed three times with phPBST, the membrane was incubated with HRP-conjugated goat antirabbit IgG for 1 h at room temperature. Finally, the membrane was incubated with the HRP-conjugated antirabbit IgG secondary antibody, developed with enhanced chemiluminescence (ECL) substrate, and visualized by Tanon 5200 Imaging Analysis System (Tanon).

Real-Time Quantitative PCR (RT-PCR). The cells were collected and total RNA was extracted using the RNAprep Pure Cell kit. mRNA was reverse-transcribed using a cDNA synthesis kit (TransGen). Reverse transcription PCR (RT-PCR) was performed using an RT-PCR Superkit (TransGen) on an Agilent Technologies Stratagene Mx3005P System. The primers for quantitative PCR were provided in Table S6. A single cycle was performed at 95 °C for 30 s, 58 °C for 30 s, and 63 °C for 30s, and this cycle was repeated 40 times. The relative transcriptional levels of target genes normalized to those of GAPDH was calculated by the comparative $2^{-\Delta\Delta}$CT method.

RNA Stability Assay. The cells were treated with 5 μg/mL actinomycin D in the presence or absence of CuB (10 μM) and then collected at the indicated time. Total RNA was extracted by RNAprep Pure Cell kit and analyzed by RT-PCR. As actinomycin D treatment results in transcription stalling, the change of mRNA concentration at a given time (dC/dt) is proportional to the constant of mRNA decay (K_{decay}) and the mRNA concentration (C), leading to the following equation.

$$dC/dt = -K_{deacy}C$$

Therefore, the mRNA degradation rate K_{decay} was estimated by $\ln(C/C_0) = -K_{deacy}t$.

To calculate the mRNA half-life ($t_{1/2}$), when 50% of the mRNA is decayed (that is, $C/C_0 = 1/2$), the equation was: $\ln(1/2) = -K_{deacy}t_{1/2}$, from where $t_{1/2} = \ln(2)/K_{decay}$.

Immunofluorescence (IF) Assay. The cells were seeded onto glass coverslips, treated with CuB for 2 h, and fixed in 4% paraformaldehyde for 30 min. After they were washed with phosphate-buffered saline (PBS) three times, cells were permeabilized with 0.1% Triton X-100 for 30 min, blocked with 5% bovine serum albumin (BSA) for 30 min at room temperature, and probed with primary antibody against IGF2BP1 (1:200) or avidin-FITC (1:200) overnight at 4 °C. Then, cells were exposed to Alexa Fluor 594-labled secondary antibodies (1:200) and stained with 4′,6-diamidino-2-phenylindole (DAPI). Image acquisition was achieved using a confocal laser scanning microscope (TCS SP8MP FLIM, Leica).

Isothermal Titration Calorimetry (ITC) Analysis. The binding affinities and thermodynamics of IGF2BP1 protein with CuB were determined using a MicroCal PEAQ-ITC (Malvern Instruments). Prior to titration, 25 μM IGF2BP1 protein was prepared in Akat buffer (50 mM sodium phosphate, pH 7.5, 100 mM NaCl). The sample cell (V = 280 μL) was filled with 25 μM IGF2BP1 protein. Titration with 0.5 mM CuB was performed at 25 °C using an initial injection of 0.4 μL followed by 12 successive injections of 2 μL with a 120 s interval. Data were analyzed by the Origin software package to determine binding parameters, including the association constant (K_D), enthalpy value (ΔH), and entropy value (ΔS).

Circular Dichroism (CD) Analysis. A CD analysis was performed using a JASCO J-810 circular dichroism spectropolarimeter (JASCO) for determining the structural changes of IGF2BP1 protein. A quartz cuvette with a path length of 1 mm was used to record CD spectra at a temperature of 298 K for 25 μM IGF2BP1 protein in the

https://doi.org/10.1021/acscentsci.2c00107
ACS Cent. Sci. 2022, 8, 1102−1115

absence or presence of CuB. Spectra were recorded over a range of 190−500 nm at 0.2 data interval with a scanning speed of 100 nm/min. Each CD spectrum represented an accumulation of three subsequent scans.

Then, all the CD measurements were performed at 25 °C with a scan speed of 100 nm/min and a response time of 1 s. Rectangular quartz cells with a 0.1 cm path length were used for scanning between 190 and 300 nm. To eliminate contributions of CuB in a CD spectrum, the same concentration of CuB (without IGF2BP1) was subtracted from the CD spectra.

Hydrogen−Deuterium Exchange Mass Spectrometry (HDX MS) Analysis. An HDX MS experiment was performed as described previously.[37] Briefly, deuterium labeling was initiated with a 20-fold dilution into D_2O buffer (50 mM sodium phosphate, pH 7.4, 100 mM NaCl) of a pre-equilibrated (30 min) aliquot of IGF2BP1 with or without CuB stock solution. After 0.25, 1, 10, 20, 60, and 240 min of labeling, the reaction was quenched with the addition of quenching buffer (37.5% hydrochloric acid). Samples were then injected and online-digested using a Waters Enzymate BEH pepsin column (2.1 × 30 mm, 5 μm). The peptides were trapped and desalted on a VanGuard Precolumn trap (Acquity UPLC BEH C18, 1.7 μm) for 3 min, eluted from the trap using 15% acetonitrile at a flow rate of 100 μL/min, and then separated using an Acquity UPLC BEH C18, 1.7 μm, 1.0 × 100 mm column. All mass spectra data were acquired using a Waters Xevo G2 mass spectrometer. Peptides were identified using ProteinLynx Global Server (PLGS) 3.0.2. Relative deuterium levels of all peptides were calculated by subtracting the mass of the undeuterated control sample from that of the deuterium-labeled sample. All mass spectra data were processed using DynamX 3.0. Deuterium levels were not corrected for back exchange and thus are reported as relative.

Establishment of Lentiviral Vector IGF2BP1-shRNA. The three highest-scoring shRNA sequences targeted for human IGF2BP1 were designed and synthesized by Hanbio Biotechnology using pHBLV-U6-MCS-CMV-ZsGreen−PGK-PURO vector (Table S7). In addition, a green fluorescent protein-tagged lentiviral vector was constructed to verify the efficiency of transfection. Empty vectors were used as a negative control. The original lentiviral vector titers contained 1.0×10^8 TU/mL.

Tumor Xenograft Experiments. IGF2BP1 wild-type or knockdown H22 cells (2×10^6) were mixed with Matrigel in a 1:1 volume on ice and then injected into the flanks of four-week-old BALB/c mice to generate xenografts. When tumors reached ∼100 mm^3 in size 7 d later, the mice received an intraperitoneal injection of CuB or 0.9% saline solution daily for 14 d. The tumor volume V was determined every day by measuring the two perpendicular diameters of the tumors and using the formula V = length (mm) × width $(mm)^2/2$, and the body weight was recorded every day. After 14 d of treatment, mice were euthanized with CO_2, and then tumors and organs (heart, liver, lung, kidney, and spleen) were weighted and fixed with 4% paraformaldehyde for further studies.

Immunohistochemistry (IHC). The HCC tissue chips and sections were deparaffinized in xylene and rehydrated to water through descending graded alcohols. Each block has a section for hematoxylin and eosin (H&E) staining. Heat-induced antigen retrieval was achieved by incubating in 0.01 M citrate buffer (pH 6.0) at 90 °C for 20 min. Attenuation of endogenous peroxidases was done by incubation in 3% hydrogen peroxide. Sections were blocked in PBS containing 10% normal goat serum and 0.3% Triton X-100 for 30 min, labeled with K_i-67 (1:200), CD4 (1:800), CD8 (1:500), CD56 (1:500), F4/80 (1:400), and PD-L1 (1:300) antibodies overnight at 4 °C and incubated with the corresponding goat secondary antibody for 1 h at room temperature. Detection was accomplished using 3,3′-diaminobenzidine (DAB) substrate kit (Solarbio). Slices were then stained with hematoxylin and examined using an Olympus IX73 instrument (Olympus). The immunostaining intensity was quantified using the Image-Pro Plus (ver. 6.0)

RNA Sequencing Assay and Functional Classification. The mRNA-seq assay was conducted by Novogene with three biological replicates. A differentially expressed gene (DEG) library was constructed for sequencing according to Illumina protocols. Briefly, total RNAs were extracted by TRIzol reagent and then purified using poly-T oligo-attached magnetic beads according to the standard protocol. Double-stranded complementary DNAs were synthesized by Superscript II reverse transcriptase. The cDNA fragments of preferentially 150−200 bp were selected by the AMPure XP system (Beckman). Clustering and sequencing were performed on a cBot Cluster Generaton System and Hiseq 2000 platform, respectively.

A differential expression analysis was performed using the DESqe R package (1.18.0). Genes with the P value less than 0.05 and $|\log_2 \text{foldchange}| > 1$ were assigned as differentially expressed. A gene ontology enrichment of DEGs was performed by Database for Annotation, Visualization, and Integrated Discovery (DAVID), including cellular component, molecular function, and biological process. A signaling pathway enrichment analysis was performed using KEGG from the CluGO program, a plug-in Cytoscape software (v.3.4.0).

Statistical Analysis. All experiments were performed at least three times. Statistical data were expressed as means ± standard deviation (SD). Comparisons between different groups were performed with a Student's t-test and analysis of variance (ANOVA) as appropriate using GraphPad Prism (ver. 8.0). Statistical comparison among groups was determined using a Kruskal−Wallis test. Values of $P < 0.05$ were considered statistically significant ($^*P < 0.05$; $^{**}P < 0.01$; $^{***}P < 0.001$).

■ ASSOCIATED CONTENT

Supporting Information

The Supporting Information is available free of charge at https://pubs.acs.org/doi/10.1021/acscentsci.2c00107.

Figure S1. IGF2BP1 plays an oncogenic role in HCC progression. Figure S2. IGF2BP1 is a direct cellular target of CuB. Figure S4. CuB directly targets IGF2BP1 via the Michael addition of thiol in cysteine to the α,β-unsaturated carbonyl. Figure S5. CuB allosterically regulates IGF2BP1-KH1−2 conformation. Figure S6. CuB reduces the m^6A mRNA stability via directly targeting IGF2BP1. Figure S7. RNA-seq profiling reveals global effects of IGF2BP1 inhibition by CuB. Figure S8. CuB inhibits HCC proliferation in vivo via inducing cell apoptosis and activating immune response. Figure S9. CuB covalently modifies IGF2BP1 at a unique Cys253 site. Figure S10. CuB regulates IGF2BP1 partners in Huh7 cells (PDF)

IGF2BP1 is a specific target in proteome profile (XLSX)

https://doi.org/10.1021/acscentsci.2c00107
ACS Cent. Sci. 2022, 8, 1102−1115

Proteome profile changes during exposure to CuB in Huh7 cells (XLSX)
Global effects of IGF2BP1 inhibition on mRNA stability (XLSX)
Primers for quantitative PCR (XLSX)
shRNA sequence for IGF2BP1 (XLSX)

AUTHOR INFORMATION

Corresponding Authors

Ke-Wu Zeng − *State Key Laboratory of Natural and Biomimetic Drugs, School of Pharmaceutical Sciences, Peking University, Beijing 100191, China;* orcid.org/0000-0003-1082-6327; Email: ZKW@bjmu.edu.cn

Peng-Fei Tu − *State Key Laboratory of Natural and Biomimetic Drugs, School of Pharmaceutical Sciences, Peking University, Beijing 100191, China*; Email: pengfeitu@bjmu.edu.cn

Authors

Yang Liu − *State Key Laboratory of Natural and Biomimetic Drugs, School of Pharmaceutical Sciences, Peking University, Beijing 100191, China; Center of Basic Medical Research, Institute of Medical Innovation and Research, Peking University Third Hospital, Beijing 100191, China*

Qiang Guo − *State Key Laboratory of Natural and Biomimetic Drugs, School of Pharmaceutical Sciences, Peking University, Beijing 100191, China*

Heng Yang − *State Key Laboratory of Natural and Biomimetic Drugs, School of Pharmaceutical Sciences, Peking University, Beijing 100191, China*

Xiao-Wen Zhang − *State Key Laboratory of Natural and Biomimetic Drugs, School of Pharmaceutical Sciences, Peking University, Beijing 100191, China*

Na Feng − *State Key Laboratory of Natural and Biomimetic Drugs, School of Pharmaceutical Sciences, Peking University, Beijing 100191, China*

Jing-Kang Wang − *State Key Laboratory of Natural and Biomimetic Drugs, School of Pharmaceutical Sciences, Peking University, Beijing 100191, China*

Ting-Ting Liu − *State Key Laboratory of Natural and Biomimetic Drugs, School of Pharmaceutical Sciences, Peking University, Beijing 100191, China*

Complete contact information is available at: https://pubs.acs.org/10.1021/acscentsci.2c00107

Author Contributions

K.-W.Z. and P.-F.T. conceived and designed the research. Y.L. performed most of the experiments. Q.G., H.Y., X.-W.Z., N.F., J.-K.W., and T.-T.L. coordinated the experiments. K.-W.Z., P.-F.T., and Y.L. wrote the manuscript. All authors contributed and reviewed the results and approved the final version of the manuscript.

Notes

The authors declare no competing financial interest.

ACKNOWLEDGMENTS

This work was financially supported by National Key R&D Program of China (2019YFC1708902, 2019YFC1711000), National Natural Sciences Foundation of China (82174008, 81973505, 2217070340), Beijing Municipal Natural Science Foundation (7222265), Peking University Medicine Seed Fund for Interdisciplinary Research (BMU2021MX023), and the State Key Laboratory of Natural and Biomimetic Drugs (K202101).

REFERENCES

(1) Demaria, O.; Cornen, S.; Daëron, M.; Morel, Y.; Medzhitov, R.; Vivier, E. Harnessing innate immunity in cancer therapy. *Nature* **2019**, *574*, 45−56.
(2) Wu, S. Y.; Fu, T.; Jiang, Y. Z.; Shao, Z. M. Natural killer cells in cancer biology and therapy. *Mol. Cancer* **2020**, *19*, 120.
(3) Bayik, D.; Lathia, J. D. Cancer stem cell-immune cell crosstalk in tumor progression. *Nat. Rev. Cancer* **2021**, *21*, 526−536.
(4) Kearney, C. J.; Vervoort, S. J.; Hogg, S. J.; Ramsbottom, K. M.; Freeman, A. J.; Lalaoui, N.; Pijpers, L.; Michie, J.; Brown, K. K.; Knight, D. A.; et al. Tumor immune evasion arises through loss of TNF sensitivity. *Sci. Immunol.* **2018**, *3*, aar3451.
(5) Martin, T. D.; Patel, R. S.; Cook, D. R.; Choi, M. Y.; Patil, A.; Liang, A. C.; Li, M. Z.; Haigis, K. M.; Elledge, S. J. The adaptive immune system is a major driver of selection for tumor suppressor gene inactivation. *Science* **2021**, *373*, 1327−1335.
(6) Agur, Z.; Elishmereni, M.; Foryś, U.; Kogan, Y. Accelerating the development of personalized cancer immunotherapy by integrating molecular patients' profiles with dynamic mathematical models. *Clin. Pharmacol. Ther.* **2020**, *108*, 515−527.
(7) Xu, Y.; Poggio, M.; Jin, H. Y.; Shi, Z.; Forester, C. M.; Wang, Y.; Stumpf, C. R.; Xue, L.; Devericks, E.; So, L.; et al. Translation control of the immune checkpoint in cancer and its therapeutic targeting. *Nat. Med.* **2019**, *25*, 301−311.
(8) Ribas, A.; Wolchok, J. D. Cancer immunotherapy using checkpoint blockade. *Science* **2018**, *359*, 1350−1355.
(9) Wang, F.; Yang, S.; Palmer, N.; Fox, K.; Kohane, I. S.; Liao, K. P.; Yu, K. H.; Kou, S. C. Real-world data analyses unveiled the immune-related adverse effects of immune checkpoint inhibitors across cancer types. *NPJ. Precis. Oncol.* **2021**, *5*, 82.
(10) Kroll, M. H.; Yee, C.; Rojas Hernandez, C. M. Hematologic complications of immune checkpoint inhibitors. *Blood* **2021** DOI: 10.1182/blood.2020009016.
(11) Liu, N.; Dai, Q.; Zheng, G. Q.; He, C.; Parisien, M.; Pan, T. N(6)-methyladenosine-dependent RNA structural switches regulate RNA-protein interactions. *Nature* **2015**, *518*, 560−564.
(12) Wang, Y.; Li, Y.; Toth, J. I.; Petroski, M. D.; Zhang, Z.; Zhao, J. C. N6-methyladenosine modification destabilizes developmental regulators in embryonic stem cells. *Nat. Cell Biol.* **2014**, *16*, 191−198.
(13) Huang, H.; Weng, H.; Sun, W.; Qin, X.; Shi, H.; Wu, H.; Zhao, B. S.; Mesquita, A.; Liu, C.; Yuan, C. L.; et al. Recognition of RNA N6-methyladenosine by IGF2BP proteins enhances mRNA stability and translation. *Nat. Cell Biol.* **2018**, *20*, 285−295.
(14) Nielsen, F. C.; Nielsen, J.; Christiansen, J. A family of IGF-II mRNA binding proteins (IMP) involved in RNA trafficking. *Scand. J. Clin. Lab. Inv. Suppl.* **2001**, *61*, 93−99.
(15) Müller, S.; Glaß, M.; Singh, A. K.; Haase, J.; Bley, N.; Fuchs, T.; Lederer, M.; Dahl, A.; Huang, H.; Chen, J.; et al. IGF2BP1 promotes SRF-dependent transcription in cancer in a m6A- and miRNA-dependent manner. *Nucleic Acids Res.* **2019**, *47*, 375−390.
(16) Kessler, S. M.; Haybaeck, J.; Kiemer, A. K. Insulin-like growth factor 2-the oncogene and its accomplices. *Curr. Pharm. Des.* **2016**, *22*, 5948−5961.
(17) Huang, X.; Zhang, H.; Guo, X.; Zhu, Z.; Cai, H.; Kong, X. Insulin-like growth factor 2 mRNA-binding protein 1 (IGF2BP1) in cancer. *J. Hematol. Oncol.* **2018**, *11*, 88.
(18) Samuels, T. J.; Järvelin, A. I.; Ish-Horowicz, D.; Davis, I. Imp/IGF2BP levels modulate individual neural stem cell growth and division through *myc* mRNA stability. *eLife* **2020**, *9*, No. e51529.
(19) Mongroo, P. S.; Noubissi, F. K.; Cuatrecasas, M.; Kalabis, J.; King, C. E.; Johnstone, C. N.; Bowser, M. J.; Castells, A.; Spiegelman, V. S.; Rustgi, A. K. IMP-1 displays cross-talk with K-Ras and modulates colon cancer cell survival through the novel proapoptotic protein CYFIP2. *Cancer Res.* **2011**, *71*, 2172−2182.
(20) Nicastro, G.; Candel, A. M.; Uhl, M.; Oregioni, A.; Hollingworth, D.; Backofen, R.; Martin, S. R.; Ramos, A. Mechanism

of β-actin mRNA recognition by ZBP1. *Cell Rep.* **2017**, *18*, 1187−1199.
(21) Bell, J. L.; Wächter, K.; Mühleck, B.; Pazaitis, N.; Köhn, M.; Lederer, M.; Hüttelmaier, S. Insulin-like growth factor 2 mRNA-binding proteins (IGF2BPs): post-transcriptional drivers of cancer progression? *Cell. Mol. Life Sci.* **2013**, *70*, 2657−2675.
(22) Nielsen, J.; Christiansen, J.; Lykke-Andersen, J.; Johnsen, A. H.; Wewer, U. M.; Nielsen, F. C. A family of insulin-like growth factor II mRNA-binding proteins represses translation in late development. *Mol. Cell. Biol.* **1999**, *19*, 1262−1270.
(23) Fakhraldeen, S. A.; Clark, R. J.; Roopra, A.; Chin, E. N.; Huang, W.; Castorino, J.; Wisinski, K. B.; Kim, T.; Spiegelman, V. S.; Alexander, C. M. Two isoforms of the RNA binding protein, coding region determinant-binding protein (CRD-BP/IGF2BP1), are expressed in breast epithelium and support clonogenic growth of breast tumor cells. *J. Biol. Chem.* **2015**, *290*, 13386−13400.
(24) Hollingworth, D.; Candel, A. M.; Nicastro, G.; Martin, S. R.; Briata, P.; Gherzi, R.; Ramos, A. KH domains with impaired nucleic acid binding as a tool for functional analysis. *Nucleic Acids Res.* **2012**, *40*, 6873−6886.
(25) Dagil, R.; Ball, N. J.; Ogrodowicz, R. W.; Hobor, F.; Purkiss, A. G.; Kelly, G.; Martin, S. R.; Taylor, I. A.; Ramos, A. IMP1 KH1 and KH2 domains create a structural platform with unique RNA recognition and remodeling properties. *Nucleic Acids Res.* **2019**, *47*, 4334−4348.
(26) Wächter, K.; Köhn, M.; Stöhr, N.; Hüttelmaier, S. Subcellular localization and RNP formation of IGF2BPs (IGF2 mRNA-binding proteins) is modulated by distinct RNA-binding domains. *Biol. Chem.* **2013**, *394*, 1077−1090.
(27) Dominissini, D.; Moshitch-Moshkovitz, S.; Schwartz, S.; Salmon-Divon, M.; Ungar, L.; Osenberg, S.; Cesarkas, K.; Jacob-Hirsch, J.; Amariglio, N.; Kupiec, M.; et al. Topology of the human and mouse m6A RNA methylomes revealed by m6A-seq. *Nature* **2012**, *485*, 201−206.
(28) Meyer, K. D.; Saletore, Y.; Zumbo, P.; Elemento, O.; Mason, C. E.; Jaffrey, S. R. Comprehensive analysis of mRNA methylation reveals enrichment in 3′ UTRs and near stop codons. *Cell* **2012**, *149*, 1635−1646.
(29) Chang, J.; Kim, Y.; Kwon, H. J. Advances in identification and validation of protein targets of natural products without chemical modification. *Nat. Prod. Rep.* **2016**, *33*, 719−730.
(30) Kenakin, T.; Miller, L. J. Seven transmembrane receptors as shapeshifting proteins: the impact of allosteric modulation and functional selectivity on new drug discovery. *Pharmacol. Rev.* **2010**, *62*, 265−304.
(31) Mahapatra, L.; Andruska, N.; Mao, C.; Le, J.; Shapiro, D. J. A novel IMP1 inhibitor, BTYNB, targets c-Myc and inhibits melanoma and ovarian cancer cell proliferation. *Transl. Oncol.* **2017**, *10*, 818−827.
(32) Müller, S.; Bley, N.; Busch, B.; Glaß, M.; Lederer, M.; Misiak, C.; Fuchs, T.; Wedler, A.; Haase, J.; Bertoldo, J. B.; et al. The oncofetal RNA-binding protein IGF2BP1 is a druggable, post-transcriptional super-enhancer of E2F-driven gene expression in cancer. *Nucleic Acids Res.* **2020**, *48*, 8576−8590.
(33) Bauer, R. A. Covalent inhibitors in drug discovery: from accidental discoveries to avoided liabilities and designed therapies. *Drug Discovery Today* **2015**, *20*, 1061−1073.
(34) Sutanto, F.; Konstantinidou, M.; Dömling, A. Covalent inhibitors: a rational approach to drug discovery. *RSC Med. Chem.* **2020**, *11*, 876−884.
(35) Massó-Vallés, D.; Beaulieu, M. E.; Soucek, L. MYC, MYCL, and MYCN as therapeutic targets in lung cancer. *Expert Opin. Ther. Targets* **2020**, *24*, 101−114.
(36) Jovanović, K. K.; Roche-Lestienne, C.; Ghobrial, I. M.; Facon, T.; Quesnel, B.; Manier, S. Targeting MYC in multiple myeloma. *Leukemia* **2018**, *32*, 1295−1306.
(37) Casey, S. C.; Tong, L.; Li, Y.; Do, R.; Walz, S.; Fitzgerald, K. N.; Gouw, A. M.; Baylot, V.; Gütgemann, I.; Eilers, M.; Felsher, D. W. MYC regulates the antitumor immune response through CD47 and PD-L1. *Science* **2016**, *352*, 227−231.
(38) Atsaves, V.; Tsesmetzis, N.; Chioureas, D.; Kis, L.; Leventaki, V.; Drakos, E.; Panaretakis, T.; Grander, D.; Medeiros, L. J.; Young, K. H.; Rassidakis, G. Z. PD-L1 is commonly expressed and transcriptionally regulated by STAT2 and MYC in ALK-negative anaplastic large-cell lymphoma. *Leukemia* **2017**, *31*, 1633−1637.
(39) Wan, Y. J.; Liao, L. X.; Liu, Y.; Yang, H.; Song, X. M.; Wang, L. C.; Zhang, X. W.; Qian, Y.; Liu, D.; Shi, X. M.; et al. Allosteric regulation of protein 14−3-3ζ scaffold by small-molecule editing modulates histone H3 post-translational modifications. *Theranostics* **2020**, *10*, 797−815.

NOTE ADDED AFTER ASAP PUBLICATION

Originally published ASAP on May 17, 2022; PDB entry number listed in Figures 3I and 4D updated on July 7, 2022.

https://doi.org/10.1021/acscentsci.2c00107
ACS Cent. Sci. 2022, 8, 1102−1115